

HIGH TEMPERATURE OXIDATION BEHAVIOUR OF NANOCRYSTALLINE  
 $\text{Fe}_{80}\text{Cr}_{20}$  ALLOYS AND FERRITIC STEEL IMPLANTED WITH  
LANTHANUM AND TITANIUM

HENDI SARYANTO

A thesis submitted in  
fulfillment of the requirement for the award of the  
Degree of Master of Mechanical Engineering

Faculty of Mechanical and Manufacturing Engineering  
Universiti Tun Hussein Onn Malaysia

October, 2011

## ABSTRACT

Fe-Cr alloys and ferritic steel have received considerable attention as Solid Oxide Fuel Cell (SOFC) interconnects material. However, the main problem with the use of Fe-Cr alloys and ferritic steels as interconnect materials is their inadequate high temperature oxidation resistance. Chromium dioxide as the protective layers becomes non protective, due to formation of crack and volatile  $\text{Cr}_2\text{O}_3$  upon exposure at high temperature oxidation. The prepared  $\text{Fe}_{80}\text{Cr}_{20}$  alloy with smallest crystallite size expected to develop a protective film of  $\text{Cr}_2\text{O}_3$  scales. On other hand, surface treatment via ion implantation technique can improve the oxidation resistance of alloys. Therefore, the purpose of this study is to investigate the oxidation resistance of implanted and unimplanted  $\text{Fe}_{80}\text{Cr}_{20}$  alloy and available commercial ferritic steel in normal atmosphere over the temperature range of 1173-1373 K. Nanocrystalline  $\text{Fe}_{80}\text{Cr}_{20}$  alloys have been produced by mechanical alloying process followed by hot compaction process. Lanthanum and titanium dopant were implanted into substrate of specimens with ion doses of  $1 \times 10^{17}$  ions/cm<sup>2</sup>. Implanted and unimplanted of specimens were subjected to oxidation at 1173 K, 1273 K, and 1373 K for 100 h. Morphology characterization of oxide scales of specimens were investigated by X-Ray Diffraction (XRD) and Scanning Electron Microscope (SEM) coupled with Energy Dispersive X-Ray analysis (EDX). The results shows that  $\text{Fe}_{80}\text{Cr}_{20}$  60 h as the smallest crystallite size exhibit better oxidation resistance. The results also indicates that the implantation of lanthanum dopant effectively reduce the growth of oxide scale as well as increases the oxidation resistance.

## ABSTRAK

Aloi Fe-Cr dan logam ferritic telah mendapat perhatian sewajarnya sebagai bahan penyambung dikenali Solid Oxide Fuel Cell (SOFC). Namun, masalah utama dalam penggunaan aloi Fe-Cr dan logam ferritic sebagai bahan penghubung ialah bahan tidak mencukupi ketahanan pengoksidaan suhu yang tinggi. Kromium dioksida yang digunakan sebagai lapisan pelindung menjadi gagal bertindak sebagai pelindung kerana pembentukan rekahan dan pemeruwapan  $\text{Cr}_2\text{O}_3$  kerana terdedah kepada suhu pengoksidaan yang tinggi. Tujuan kajian ini adalah untuk membangunkan struktur nanocrystalline baru pada aloi  $\text{Fe}_{80}\text{Cr}_{20}$  yang dibandingkan dengan logam ferritic komersial, kemudian diteruskan dengan rawatan permukaan melalui teknik pengimplanan ion bagi penerapan pada suhu yang tinggi. Nanocrystalline  $\text{Fe}_{80}\text{Cr}_{20}$  telah di hasilkan melalui proses pengalioian mekanikal diikuti dengan proses pemampatan. Dopan lanthanum dan titanium diimplan kepada substrat specimen dengan dos ion  $1 \times 10^{17}$  ions/cm<sup>2</sup>. specimen yang diimplan dan tidak diimplan didedahkan kepada pengoksidaan pada 1173, 1273 dan 1373 K selama 100 h. Skala oksida bagi karakter morfologi untuk specimen dikaji menggunakan X-Ray Diffraction (XRD) dan Scanning Electron Microscope (SEM) bersama-sama dengan analisis Energy Dispersive X-Ray (EDX). Hasil kajian menunjukkan specimen yang mempunyai saiz nano yang lebih halus ( $\text{Fe}_{80}\text{Cr}_{20}$  alloy dengan masa pengisaran 60 jam) menunjukkan prestasi yang terbaik dalam memperbaiki rintangan suhu pengoksidaan. Hasil kajian juga menunjukkan implantasi lanthanum dopan berkesan untuk mengurangkan pertumbuhan skala oksida dan memperbaiki rintangan suhu pengoksidaan.

## CONTENTS

<b>TITLE</b>	<b>i</b>
<b>DECLARATION</b>	<b>ii</b>
<b>ACKNOWLEDGEMENT</b>	<b>iv</b>
<b>ABSTRACT</b>	<b>v</b>
<b>CONTENTS</b>	<b>vii</b>
<b>LIST OF TABLES</b>	<b>xiv</b>
<b>LIST OF FIGURES</b>	<b>xvi</b>
<b>LIST OF SYMBOLS AND ABBREVIATIONS</b>	<b>xxii</b>
<b>LIST OF APPENDICES</b>	<b>xxiv</b>
 <b>CHAPTER 1 INTRODUCTION</b>	 <b>1</b>
1.1 Research background	1
1.1.1 Types of fuel cells	2
1.1.2 Solid oxide fuel cells	3
1.1.3 SOFC interconnects	5
1.1.4 Potential Metallic alloys as interconnects	5

1.2	Problem statement	6
1.3	Hyphothesis	7
1.4	The research aim	7
1.5	Research objectives	7
1.6	Scopes of study	7
<b>CHAPTER 2 LITERATURE REVIEW</b>		<b>22</b>
2.1	Introduction of solid oxide fuel cell	9
2.2	Operating principle of SOFC	11
2.3	SOFC components	11
2.3.1	Cathode	12
2.3.2	Anode	12
2.3.3	Electrolyte	13
2.3.4	Interconnect	13
2.4	SOFC interconnect materials	15
2.4.1	Ceramic interconnect	15
2.4.2	Metallic inteconnects	17
2.4.2.1	Chromium based alloys	18
2.4.2.2	Iron based alloys	19

2.5	Fabrication process of metallic interconnects	20
2.5.1	Powder metallurgy route	21
2.5.2	Mechanical alloying	22
2.5.3	Development of nanocrystalline alloys by mechanical alloying process	26
2.5.4	Metal powder compaction	28
2.5.4.1	Hot compaction	28
2.5.4.2	Compacting temperatures	30
2.6	Surface modification via ion implantation technique	32
2.7	Effect of reactive elements upon oxidation	35
2.8	High temperature oxidation	37
2.8.1	Oxidation resistance	38
2.8.2	Oxidation resistance of metallic alloys	39
2.8.3	Oxidation resistance of nanocrystalline iron chromium alloys	40
2.8.4	The Wagner's oxidation theory	41
2.8.5	Thermodynamically stable of oxide phases	44

2.9	Summary of literature reviews	47
-----	-------------------------------	----

## **CHAPTER 3 METHODOLOGY** **48**

3.1	Preparation of ball milled Fe <sub>80</sub> Cr <sub>20</sub> powders	48
3.2	Mechanical alloying process	49
3.3	Powder consolidation of ball milled powders	50
3.4	Microstructural characterization of unmilled and ball milled powder	51
3.4.1	X-ray diffraction peaks profiling analysis of ball milled powders	51
3.4.2	Morphology characterization of ball milled powders	54
3.4.3	Phase analysis of ball milled powders	55
3.4.4	TEM observation of ball milled powders	56
3.5	Chemical composition analysis of commercial ferritic steel	56
3.6	Surface treatment via ion implantation process	57
3.6.1	Preparation of ion implantation process	58
3.6.2	Ion implantation proses	59
3.6.3	Ion implantation depth distribution analysis	59

3.7	Experimental procedures for high temperature oxidation test	60
3.8	Evaluation of high temperature oxidation test	61
3.8.1	Oxidation kinetics	61
3.8.2	Surface morphology characterization of oxide scale	62
3.8.3	Identification of oxide phases	62
3.8.4	Cross-section analysis of oxide scale	63
3.9	Flow chart	64
<b>CHAPTER 4 RESULTS AND DISCUSSION</b>		<b>66</b>
4.1	Synthesis characterization of unmilled powders (Fe and Cr)	66
4.2	Synthesis characterization of ball milled $\text{Fe}_{80}\text{Cr}_{20}$ powders	67
4.2.1	Measuring crystallite size of unmilled and ball milled powders	68
4.2.2	Morphology characterization of ball milled $\text{Fe}_{80}\text{Cr}_{20}$ powders	71
4.2.3	Validation of nanocrystalline structure of ball milled $\text{Fe}_{80}\text{Cr}_{20}$ powders using TEM observation	72



4.3	Phase analysis of ball milled Fe <sub>80</sub> Cr <sub>20</sub> powders	74
4.4	Microstructural characterization of consolidated Fe <sub>80</sub> Cr <sub>20</sub> alloys compared to commercial ferritic steel	77
4.5	Chemical composition analysis of commercial ferritic steel	78
4.6	Measuring crystallite size of Fe <sub>80</sub> Cr <sub>20</sub> alloys as consolidated specimens compared to commercial ferritic steel	79
4.7	Synthesis evaluation of lanthanum and titanium implantation into substrate of the specimens	81
4.8	High temperature oxidation test	84
4.8.1	The effect of nanocrystalline structure on the oxidation kinetic of Fe <sub>80</sub> Cr <sub>20</sub> alloys and commercial ferritic steel	84
4.8.2	Surface scale morphology of Fe <sub>80</sub> Cr <sub>20</sub> alloys compare to commercial ferritic steel after oxidation at 1173, 1273 and 1373 K	89
4.8.3	The effect of lanthanum and titanium implantation on the oxidation behavior of Fe <sub>80</sub> Cr <sub>20</sub> alloys and commercial ferritic steel	94
4.8.4	Surface scale morphology of implanted specimens compare to unimplanted specimens after oxidation at 1173, 1273 and 1373 K	99

4.9	Identification of oxide phase	104
4.10	Cross-sectional morphology of the oxide scale	109
4.10.1	Cross-sectional analysis of un-implanted and implanted Fe <sub>80</sub> Cr <sub>20</sub> alloy after oxidation in air at 1173 K for 100 hours	119
4.10.2	Cross-sectional analysis of un-implanted and implanted Fe <sub>80</sub> Cr <sub>20</sub> alloy after oxidation in air at 1273 K for 100 hours	112
4.10.3	Cross-sectional analysis of un-implanted and implanted Fe <sub>80</sub> Cr <sub>20</sub> alloy after oxidation in air at 1373 K for 100 hours	116
<b>CHAPTER 5 CONCLUSIONS AND RECOMENDATIONS</b>		<b>119</b>
5.1	Conclusion	119
5.2	Recomendation	120
<b>REFERENCES</b>		<b>121</b>
<b>APPENDICES</b>		<b>133</b>
<b>VITA</b>		

## LIST OF TABLES

1.1	The main characteristics of different types of fuel cells	2
2.1	Sintering temperature and time ranges of commonly used P/M metals and alloys	31
3.1	Parameter of ball milled powders	50
4.1	Peak width and peak intensity of as starting powders (pure Fe and Cr powders) and ball milled $\text{Fe}_{80}\text{Cr}_{20}$ powders	68
4.2	Evaluation of starting materials of $\text{Fe}_{80}\text{Cr}_{20}$ as the ball milled powders	70
4.3	The lattice parameter of pure Fe and Cr powders as starting materials	74
4.4	Lattice parameter calculations for the ball milled $\text{Fe}_{80}\text{Cr}_{20}$	74
4.5	The solubility Cr into Fe (Solid solubility)	75
4.6	Chemical composition of commercial ferritic steel obtained by Glow discharge spectrometry (GDS)	78
4.7	Peaks width and peaks intensity of $\text{Fe}_{80}\text{Cr}_{20}$ alloys and ferritic steel as consolidated and as received specimens	80
4.8	Crystallite size and strain of $\text{Fe}_{80}\text{Cr}_{20}$ alloys and ferritic steel as consolidated and as received specimens	80
4.9	The projected range (Ion range $R_p$ ) and longitudinal straggle $\sigma R_p$ of lanthanum and titanium implantation in to substrate of the specimens	83
4.10	The effect of nanocrystalline structure on the weight gains of specimens after oxidation at 1173, 1273 and 1373 K in air for 100 h	88
4.11	Comparison parabolic rate constant ( $k_p$ ) of specimens after oxidation at three various temperatures (1173, 1273 and 1373 K) for 100 h	88

4.12	Composition of $\text{Cr}_2\text{O}_3$ and $\text{FeO}$ on the surface scale of specimens after oxidation at 1173, 1273 and 1373 K	93
4.13	Partial pressure ( $\text{P}_{\text{O}_2}$ ) and Gibbs energy ( $\Delta G^\circ$ ) of oxide types	105
4.14	Composition of oxide scale on the surface of specimens at 1173 K	110
4.15	Composition of oxide scale on the surface of specimens at 1273 K	113
4.16	Composition of oxide scale on the surface of specimens at 1373 K	117



## LIST OF FIGURES

1.1	SOFC principles of operation	3
1.2	Planar and Tubular design of solid oxide fuel cell	4
2.1	Operating principle of solid oxide fuel cell	10
2.2	Design for solid oxide fuel cell	11
2.3	Ball-powder-ball collision of powder mixture during mechanical alloying	23
2.4	Average grain size (filled symbols) and atomic-level strain (open symbols) for $\text{Ni}_x\text{Al}_{100-x}$ powders after 100 h of milling as a function of composition	27
2.5	Average grain size obtained for $\text{Ni}_{56}\text{Al}_{54}$ and $\text{Ni}_{60}\text{Al}_{40}$ powders after 100 h of ball milling and after addition of elemental Ni or Al and subsequent mechanical alloying as a function of total milling time	27
2.6	Schematic design of hot pressing unit	28
2.7	Schematic of hot compaction process	29
2.8	Binary Fe-Cr equilibrium phase diagram	30
2.9	Typical temperature-time profile for Powder Metallurgy steel parts during sintering	30
2.10	Schematic of an ion implantation system	33
2.11	Schematic of the ion implantation process	34
2.12	Isothermal oxidizing mass gain curves of $\text{Co}_{60}\text{Cr}_{40}$ and La implanted $\text{Co}_{60}\text{Cr}_{40}$	36
2.13	Oxidation kinetics of nanocrystalline and microcrystalline Fe-10Cr alloys, oxidised at 300°C (573 K): (a) weight-gain vs time plots for 3120 minutes	40
2.14	Parabolic kinetics for microcrystalline alloy compared with parabolic kinetics for nanocrystalline alloy	41

2.15	Diagram of scale formation according to Wagner's model	42
2.16	Standard free energy of formation of selected oxides as a function of temperature	46
3.1	Glove Box	48
3.2	Hardened steel vial	49
3.3	RETCHEM PM400 planetary ball mill	49
3.4	Cycle of consolidation process	50
3.5	A straight line with a slope of $4\varepsilon$ and an intercept of $K\lambda/D$	53
3.6	FWHM of the standard reference material for $\text{LaB}_6$	53
3.7	X-Ray powder diffraction-BRUKER D8 ADVANCE	54
3.8	Scanning Electron Microscope (SEM) JSM-6380LA	54
3.9	Transmission Electron Microscope-JEM-2100, 200kV	55
3.10	LECO Glow Discharge Spectrometry 850A	57
3.11	Cockcroft-Walton accelerator Type 200 keV/200 $\mu\text{A}$	57
3.12	Polishing machine	58
3.13	Apparatus for Archimedes test	58
3.14	CARBOLITE box furnace	60
3.15	Cyclic of oxidation tests of implanted and un-implanted specimens among temperature of 1173, 1273 and 1373 K for 100 hours	60
3.16	Fe-Cr - $p(\text{O}_2)$ phase diagram for 1173 K	62
3.17	Fe-Cr - $p(\text{O}_2)$ phase diagram for 1273 K	63
3.18	Fe-Cr - $p(\text{O}_2)$ phase diagram for 1373 K	63
3.19	Flow chart	65
4.1	Diffraction peaks of pure Fe and Cr	66
4.2	Diffraction peaks of $\text{Fe}_{80}\text{Cr}_{20}$ system as milled powders	67
4.3	Crystallite size vs Milling time	69
4.4	SEM micrograph of ball-milled $\text{Fe}_{80}\text{Cr}_{20}$ powders in early stage of milling times : (a) $\text{Fe}_{80}\text{Cr}_{20}$ 7 h, (b) $\text{Fe}_{80}\text{Cr}_{20}$ 15 h	70
4.5	SEM micrograph of ball-milled $\text{Fe}_{80}\text{Cr}_{20}$ powders: (a) $\text{Fe}_{80}\text{Cr}_{20}$ 20 h, (b) $\text{Fe}_{80}\text{Cr}_{20}$ 40 h, (c) $\text{Fe}_{80}\text{Cr}_{20}$ 60 h and (d). $\text{Fe}_{80}\text{Cr}_{20}$ 80 h	70
4.6	Plan view TEM micrographs of ball-milled $\text{Fe}_{80}\text{Cr}_{20}$ powders: (a) $\text{Fe}_{80}\text{Cr}_{20}$ 40 h and (b) $\text{Fe}_{80}\text{Cr}_{20}$ 60 h	73
4.7	Variation of the lattice parameter of the ball milled $\text{Fe}_{80}\text{Cr}_{20}$ with different milling time	75

4.9	Identification of phase alloy for the ball milled $\text{Fe}_{80}\text{Cr}_{20}$ 60 h at $44.523^\circ$	76
4.10	One of the selected $\text{Fe}_{80}\text{Cr}_{20}$ alloys as consolidated specimens	77
4.11	Surface morphology characterization of $\text{Fe}_{80}\text{Cr}_{20}$ alloys and ferritic steel as consolidated and as received specimens	78
4.12	Diffraction peaks of $\text{Fe}_{80}\text{Cr}_{20}$ alloys and ferritic steel as consolidated and as received specimens	79
4.13	The projected range ( $R_p$ ) of lanthanum implantation into substrate of: (a) $\text{Fe}_{80}\text{Cr}_{20}$ 40 h, (b) $\text{Fe}_{80}\text{Cr}_{20}$ 60 h, (c) $\text{Fe}_{80}\text{Cr}_{20}$ 80 h and (d) Ferritic steel	81
4.14	The projected range ( $R_p$ ) of titanium implantation into substrate of: (a) $\text{Fe}_{80}\text{Cr}_{20}$ 40 h, (b) $\text{Fe}_{80}\text{Cr}_{20}$ 60 h, (c) $\text{Fe}_{80}\text{Cr}_{20}$ 80 h and (d) Ferritic steel	82 71
4.15	The effect of crystallite size on the weight gains of $\text{Fe}_{80}\text{Cr}_{20}$ alloys compared to commercial ferritic steel after oxidation at 1173 K in air for 100 h	84 72
4.16	The effect of crystallite size on the weight gains of $\text{Fe}_{80}\text{Cr}_{20}$ alloys compared to commercial ferritic steel after oxidation at 1273 K in air for 100 h	85
4.17	The effect of crystallite size on the weight gains of $\text{Fe}_{80}\text{Cr}_{20}$ alloys compared to commercial ferritic steel after oxidation at 1373 K in air for 100 h	85
4.18	Parabolic rate constants ( $k_p$ ) of the $\text{Fe}_{80}\text{Cr}_{20}$ alloys compared to commercial ferritic steel after oxidation at 1173 K in air for 100 h	86
4.19	Parabolic rate constants ( $k_p$ ) of the $\text{Fe}_{80}\text{Cr}_{20}$ alloys compared to commercial ferritic steel after oxidation at 1273 K in air for 100 h	87
4.20	Parabolic rate constants ( $k_p$ ) of the $\text{Fe}_{80}\text{Cr}_{20}$ alloys compared to commercial ferritic steel after oxidation at 1373 K in air for 100 h Surface scale morphology of specimens at 1173 K after 100 h	87
4.21	exposed to air: (a) $D = 53.32$ nm ( $\text{Fe}_{80}\text{Cr}_{20}$ 40 h); (b) $D = 38.51$ nm ( $\text{Fe}_{80}\text{Cr}_{20}$ 60 h); (c) $D = 76.30$ nm ( $\text{Fe}_{80}\text{Cr}_{20}$ 80 h) and (d) $D = 77.30$ nm (Commercial ferritic steel)	89

4.22	Surface scale morphology of specimens at 1273 K after 100 h exposed to air: (a) $D = 53.32$ nm ( $\text{Fe}_{80}\text{Cr}_{20}$ 40 h); (b) $D = 38.51$ nm ( $\text{Fe}_{80}\text{Cr}_{20}$ 60 h); (c) $D = 76.30$ nm ( $\text{Fe}_{80}\text{Cr}_{20}$ 80 h) and (d) $D = 77.30$ nm (Commercial ferritic steel)	90
4.23	Surface scale morphology of specimens at 1373 K after 100 h exposed to air: (a) $D = 53.32$ nm ( $\text{Fe}_{80}\text{Cr}_{20}$ 40 h); (b) $D = 38.51$ nm ( $\text{Fe}_{80}\text{Cr}_{20}$ 60 h); (c) $D = 76.30$ nm ( $\text{Fe}_{80}\text{Cr}_{20}$ 80 h) and (d) $D = 77.30$ nm (Commercial ferritic steel)	91
4.24	Effect of lanthanum and titanium implantation on weight gains of specimens after oxidation in air for 100 h at 1173 K compared to unimplanted specimens	94
4.25	Parabolic rate constant of the implanted specimens compared to unimplanted specimens after oxidation in air for 100 h at 1173 K	95
4.26	Effect of lanthanum and titanium implantation on weight gains of specimens after oxidation in air for 100 h at 1273 K compared to unimplanted specimens	96
4.27	Parabolic rate constant of the implanted specimens compared to unimplanted specimens after oxidation in air for 100 h at 1273 K	97
4.28	Effect of lanthanum and titanium implantation on weight gains of specimens after oxidation in air for 100 h at 1373 K compared to unimplanted specimens	97
4.29	Parabolic rate constant of the implanted specimens compared to unimplanted specimens after oxidation in air for 100 h at 1373 K	98
4.30	SEM micrograph of the top scale surface that formed at 1173 K after 100 h exposed to air: (a) Unimplanted $\text{Fe}_{80}\text{Cr}_{20}$ alloy; (b) $\text{Fe}_{80}\text{Cr}_{20}$ alloy implanted La and (c) $\text{Fe}_{80}\text{Cr}_{20}$ alloy implanted Ti	99
4.31	SEM micrograph of the top scale surface that formed at 1173 K after 100 h exposed to air: (a) Unimplanted commercial ferritic steel; (b) commercial ferritic steel implanted with La and (c) commercial ferritic steel implanted with Ti	100



4.32	SEM micrograph of the top scale surface that formed at 1273 K after 100 h exposed to air: (a) Unimplanted Fe <sub>80</sub> Cr <sub>20</sub> alloy; (b) Fe <sub>80</sub> Cr <sub>20</sub> alloy implanted La and (c) Fe <sub>80</sub> Cr <sub>20</sub> alloy implanted Ti	101
4.33	SEM micrograph of the top scale surface that formed at 1273 K after 100 h exposed to air: (a) Unimplanted commercial ferritic steel; (b) commercial ferritic steel implanted La and (c) commercial ferritic steel implanted Ti	102
4.34	SEM micrograph of the top scale surface that formed at 1373 K after 100 h exposed to air: (a) Unimplanted Fe <sub>80</sub> Cr <sub>20</sub> alloy; (b) Fe <sub>80</sub> Cr <sub>20</sub> alloy implanted La and (c) Fe <sub>80</sub> Cr <sub>20</sub> alloy implanted Ti	102
4.35	SEM micrograph of the top scale surface that formed at 1373 K after 100 h exposed to air: (a) Unimplanted commercial ferritic steel; (b) commercial ferritic steel implanted La and (c) commercial ferritic steel implanted Ti	103
4.36	XRD pattern of the oxide phase for implanted and unimplanted Fe <sub>80</sub> Cr <sub>20</sub> alloy compare to commercial ferritic steel at 1173 K	106
4.37	XRD pattern of the oxide phase for implanted and unimplanted Fe <sub>80</sub> Cr <sub>20</sub> alloy compare to commercial ferritic steel at 1273 K	107
4.38	XRD pattern of the oxide phase for implanted and unimplanted Fe <sub>80</sub> Cr <sub>20</sub> alloy compare to commercial ferritic steel at 1373 K	108
4.39	Cross-sectional morphology of specimens after oxidation in air at 1173 K for 100 hours: (a) Fe <sub>80</sub> Cr <sub>20</sub> alloy (un-implanted), (b) Fe <sub>80</sub> Cr <sub>20</sub> alloy implanted La and (c) Fe <sub>80</sub> Cr <sub>20</sub> alloy implanted Ti	109
4.40	Elemental mapping cross-sectional of un-implanted Fe <sub>80</sub> Cr <sub>20</sub> alloy after oxidation in air at 1173 K for 100 hours	111
4.41	Elemental mapping cross-sectional of Fe <sub>80</sub> Cr <sub>20</sub> alloy implanted La after oxidation in air at 1173 K for 100 hours	111
4.42	Elemental mapping cross-sectional of Fe <sub>80</sub> Cr <sub>20</sub> alloy implanted Ti after oxidation in air at 1173 K for 100 hours	112
4.43	Cross-sectional morphology of specimens after oxidation in air at 1273 K for 100 hours: (a) Fe <sub>80</sub> Cr <sub>20</sub> alloy (un-implanted), (b) Fe <sub>80</sub> Cr <sub>20</sub> alloy implanted La and (c) Fe <sub>80</sub> Cr <sub>20</sub> alloy implanted Ti	113
4.44	Elemental mapping cross-sectional of un-implanted Fe <sub>80</sub> Cr <sub>20</sub> alloy after oxidation in air at 1273 K for 100 hours	114

4.45	Elemental mapping cross-sectional of Fe <sub>80</sub> Cr <sub>20</sub> alloy implanted La after oxidation in air at 1273 K for 100 hours	115
4.46	Elemental mapping cross-sectional of Fe <sub>80</sub> Cr <sub>20</sub> alloy implanted Ti after oxidation in air at 1273 K for 100 hours	115
4.47	Cross-sectional morphology of specimens after oxidation in air at 1373 K for 100 hours: (a) Fe <sub>80</sub> Cr <sub>20</sub> alloy (unimplanted), (b) Fe <sub>80</sub> Cr <sub>20</sub> alloy implanted La and (c) Fe <sub>80</sub> Cr <sub>20</sub> alloy implanted Ti	116
4.48	Elemental mapping cross-sectional of un-implanted Fe <sub>80</sub> Cr <sub>20</sub> 60 h after oxidation in air at 1373 K for 100 hours	117
4.49	Elemental mapping cross-sectional of Fe <sub>80</sub> Cr <sub>20</sub> 60 h implanted La after oxidation in air at 1373 K for 100 hours	118
4.50	Elemental mapping cross-sectional of Fe <sub>80</sub> Cr <sub>20</sub> 60 h implanted Ti after oxidation in air at 1373 K for 100 hours	118



## LIST OF APPENDICES

A	X-RAY DIFFRACTION PATTERN OF STARTING MATERIALS	131
B	X-RAY DIFFRACTION ANALYSIS	144
C	VALIDATION OF NANOCRYSTALLINE STRUCTURE OF THE BALL MILLED $\text{Fe}_{80}\text{Cr}_{20}$ POWDERS USING TEM OBSERVATION	157
D	ION IMPLANTATION RESULTS	159
E	THE COMPARISON OF THE OXIDATION KINETICS OF IMPLANTED SPECIMENS WITH UNIMPLANTED SPECIMENS	166
F	SURFACE SCALE MORPHOLOGY OF UNIMPLANTED AND IMPLANTED SPECIMENS	174
G	MEASURING OXYGEN PARTIAL PRESSURE ( $P_{O_2}$ ) AND GIBBS ENERGY ( $\Delta G^\circ$ ) OF OXIDE TYPES	193
H	IDENTIFICATION OF OXIDE PHASE	196
I	IDENTIFICATION OF OXIDE PHASE THAT FORMED ON THE OXIDE SCALE OF SPECIMENS AFTER OXIDATION AT THREE VARIOUS TEMPERATURES (1173, 1273 AND 1373 K)	196 200
J	PAPER PUBLICATION	210

## LIST OF SYMBOLS AND ABBREVIATIONS

$\alpha$	- Alpha
$\gamma$	- Gamma
$\lambda$	- Wavelength
$\theta$	- Diffraction angle
$\varepsilon$	- Strain
$\Delta G$	- Gibbs energy
$\Delta W$	- Mass gain change
$\sigma_{Rp}$	- Longitudinal straggling
$A$	- Surface area
$a_1$	- The lattice parameter of the pure solvent element
$a_2$	- The lattice parameter of solute element
$a_{ss}$	- The lattice parameter of solid solubility and $x$ is the solid solubility
$B_{corrected}$	- The instrumental corrected full width at half maximum (FWHM)
$B_{inst}$	- FWHM of the standard reference materials
$B_{observed}$	- The full width at half maximum (FWHM) from diffraction peaks of the specimens
Cr	- Chromium
Cr <sub>2</sub> O <sub>3</sub>	- Chromium dioxide
CT	- Cycle Time
$D$	- Crystallite size
$d$	- Interplanar spacing
EDX	- Energy-dispersive X-ray spectroscopy
Fe	- Iron
Fe <sub>2</sub> O <sub>3</sub>	- Iron oxide
Fe <sub>80</sub> Cr <sub>20</sub> 7 h	- 80wt%Fe and 20wt%Cr with milling time 7 hours
Fe <sub>80</sub> Cr <sub>20</sub> 15 h	- 80wt%Fe and 20wt%Cr with milling time 15 hours

$\text{Fe}_{80}\text{Cr}_{20}$ 20 h	- 80wt%Fe and 20wt%Cr with milling time 20 hours
$\text{Fe}_{80}\text{Cr}_{20}$ 40 h	- 80wt%Fe and 20wt%Cr with milling time 40 hours
$\text{Fe}_{80}\text{Cr}_{20}$ 60 h	- 80wt%Fe and 20wt%Cr with milling time 60 hours
$\text{Fe}_{80}\text{Cr}_{20}$ 80 h	- 80wt%Fe and 20wt%Cr with milling time 80 hours
FWHM	- Full width at half maximum
ICDD PDF-2	- International standard diffraction data
$K$	- Scherrer constant
$k_p$	- Parabolic rate constant
La	- Lanthanum
$\text{LaCrO}_3$	- Lanthanum chromite
$\text{LaB}_6$	- Lanthanum Hexaboride
MT	- Milling time
$p\text{O}_2$	- Oxygen partial pressure
PT	- Pause time
Rp	- Ion range
S	- Time oxidation (hours)
SEM	- Scanning Electron Microscope
SOFCs	- Solid oxide fuel cells
t	- Time
Ti	- Titanium
UTHM	- Universiti Tun Hussein Onn Malaysia
$W_0$	- Mass before oxidation
$W_t$	- Mass after oxidation
$x_i$	- The depth penetration of implanted ions
XRD	- X-Ray Diffractometer
YSZ	- Yttria stabilised zirconia

## CHAPTER I

### INTRODUCTION

In this chapter, the background and premise of the research will be explained which consists of the research background focusing towards the research study, problem statement, hypothesis, research aim, objective study, scope and the significance of the research.

#### 1.1 Research background

Fuel cells are devices that produce electrical energy through electrochemical processes, without combusting fuel and generating pollution of the environment. They represent a potential source of energy for a wide variety of applications (Ion & Loyalka, 2007). The basic physical structure of fuel cell consists of an electrolyte layer in contact with an porous anode and cathode on either side. In typical a fuel cell, gaseous fuels are fed continuously to the anode (negative electrode) and oxidant (i.e. oxygen from air) is feed continuously to the cathode (positive electrode), electrochemical reactions take a place at the electrodes to produces an electrical current (Hirschenhofer *et al.*, 1998).

### 1.1.1 Types of fuel cells

At present, there are five main types of fuel cells according to different electrolyte materials. They are the polymer electrolyte fuel cell (PEFC), the phosphoric acid fuel cell (PAFC), the molten carbonate fuel cell (MCFC), the alkaline fuel cell (AFC) and the solid oxide fuel cell (SOFC). The main characteristics of these fuel cells are summarized in Table 1.1.

Although AFC is the oldest fuel cell and it provides extremely high power density, it is considered to be impractical because of the need to remove trace  $\text{CO}_2$  from both the fuel and oxidant streams in order to prevent reaction of the electrolyte to form solid, non-conducting alkali carbonates. Furthermore the strong alkaline solution presents a number of problems. PAFC is the most advance fuel cell at the present stage. The high manufacture cost, however, prevents its commercialization. PEFC has recently attracted significant attention as a potential source of primary power in transportation application and worldwide investment in PEFC continues to grow. Given their high temperatures of operation, MCFC has great applicability in stationary power generation. But it suffers from the difficulties of containing a corrosive liquid electrolyte. In particular, dissolution of NiO at the cathode and its precipitation in the form of Ni at the anode can result in electrical shorts across the electrolyte (Yamamoto, 2000; Ormerod, 2003; Haile, 2003). Although in public eyes, SOFC is not as prominent as PEFC, it has many advantages such as multi-fuel capability and simplicity of system design. Moreover, the exhaust heat can be used as a heat source for a variety of processes (Yamamoto, 2000).

Table 1.1: The main characteristics of different types of fuel cells (Haile, 2003)

Parameter	Fuel cells type				
	AFC	PEFC	PAFC	MCFC	SOFC
Temperature K	333-393	343-353	493	923-1023	1073-1273
Electrolyte	KOH	Solid Polymer	Phosphoric acid	Lithium	Solid oxide
Fuel	Pure $\text{H}_2$	$\text{H}_2$	$\text{H}_2$	$\text{H}_2$ , CO, $\text{CH}_4$	$\text{H}_2$ , CO, Hydrocarbon
Efficiency %	33-55	30-40	40	>50	>50
Max power (kW)	5	250	200	1000	1000

### 1.1.2 Solid oxide fuel cells

Among various types of fuel cell, solid oxide fuel cells (SOFCs) has attracted considerable interest as it offers wide application ranges, the solid oxide fuel cells seem the most efficient way to generate electricity from a variety of fuel such as hydrogen, methane or even natural gases owing to their high operating temperatures typically in the range 1073-1273 K for conversion of chemical fuels directly into electrical power (Singhal & Kendal, 2003; Quadakkers *et al.*, 2003).

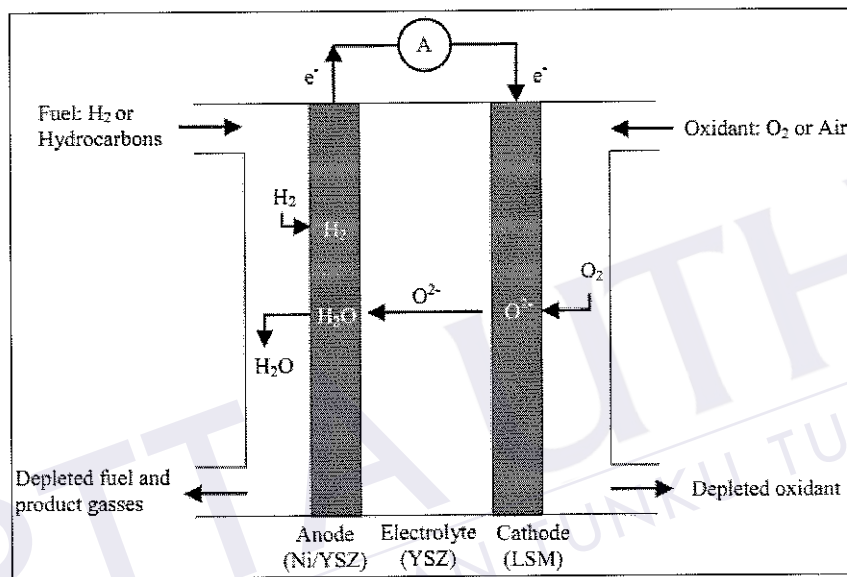


Figure 1.1: SOFC principles of operation (Stambouli & Traversa, 2002)

A solid oxide fuel cell is made up of four layers, three of which are ceramics. A single cell consisting of these four layers stacked together is typically only a few millimeters thick. Hundreds of these cells are then connected in series to form what most people refer to as an "SOFC stack". Figure 1.1 shows an SOFC scheme. It contains a solid oxide electrolyte, where in typically made from a ceramic such as yttria-stabilised zirconia (YSZ) which acts as a conductor of oxide ions. Ni-YSZ cermets are the most commonly used anode materials for SOFCs. Ni is an excellent catalyst for fuel oxidation. Conducting perovskites are the preferred cathode materials. Lanthanum manganite (LaMnO<sub>3</sub>), which, when substituted with low valence elements such as Ca or Sr, has good type electronic conduction. Moreover,



doped  $\text{LaMnO}_3$  possesses adequate electrocatalytic activity, a reasonable thermal expansion match to YSZ, and stability in the SOFC cathode operating environment (Singhal & Kendal, 2003). Since a single cell only produces voltage less than 1 V and power around  $1 \text{ W/cm}^2$ , many cells are electrically connected together in a cell stack to obtain higher voltage and power (Singhal, 2007).

Several technical issues have been identified and are being addressed in the development of SOFC products for practical applications. These issues mainly relate to competitive cost and reliable performance with desired operating characteristics. The development of suitable low cost materials and the low cost fabrication of material structures, with the aim of obtaining a higher and more stable electrochemical performance are presently the key technical challenges facing SOFC's (Singhal, 2000; Quadackers *et al.*, 2003).

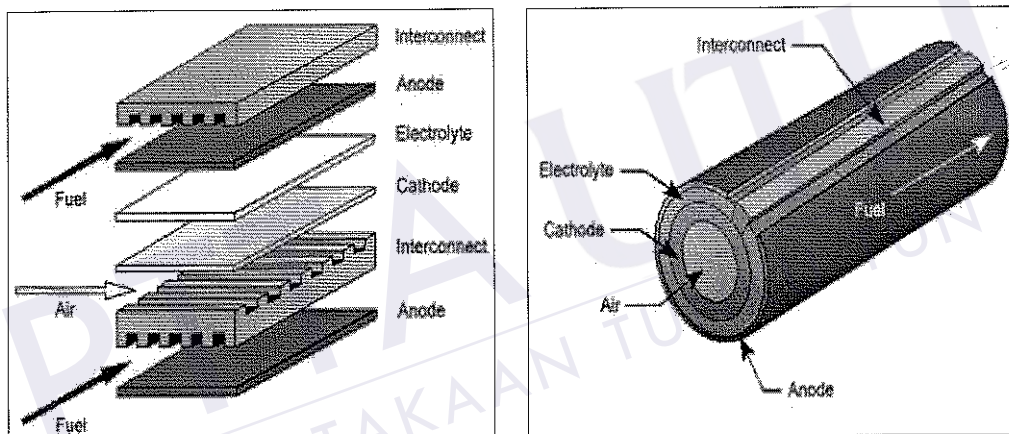


Figure 1.2: Planar and Tubular design of solid oxide fuel cell (Singhal, 2004)

Construction of the planar and tubular types SOFC require application of an interconnector to join the anode of one cell with the cathode of the next cell in a voltage stack as shown in Figure 1.2. For these reasons, the interconnector is a key element for the functioning and long-term reliability of SOFC.

## REFERENCES

- Angelo, P.C. & Subramanian, R. (2008). *Powder Metallurgy: Science, Technology and Applications*. New Delhi: PHI Learning Private Limited.
- Anders, A. (2001). *Handbook of Plasma Immersion Ion Implantation and Deposition*. New York: John Willey & Sons.
- Basu, R.N. (2007). *Materials for Solid Oxide Fuel Cells*. New Delhi: Anamaya Publishers
- Becker, B.S, Bolton, J.D. & Eagles, A.M. (2000). Sintering of 316L stainless steels to high density via the addition of chromium–molybdenum dibromide Powders Part 1: Sintering performance and mechanical properties, *Journal of Materials Design and Applications*, 214(3), pp. 139-152.
- Bergman, O. (2008). *Studies of Oxide Reduction and Nitrogen Uptake in Sintering of Chromium-alloyed Steel Powder*, Kungliga Tekniska Högskolan, Master Thesis.
- Birks, N., Meier, G.H. & Pettit, F.S. (Eds.) (2006). *Introduction to the High Temperature Oxidation of Metals*. New York: Cambridge University Press.
- Black, J.T. & Kohser, R.A. (Eds.) (2007). *DeGarmo's Materials and Processes in Manufacturing*. United State of America: John Wiley & Sons. Ltd.

- Bridgeman, J.T., Marker, V.A., Hummel, S.K., Benson, B.W. & Pace, L.L. (1997). Comparison of titanium and cobalt-chromium removable partial denture clasps. *Journal of Prosthetic Dentistry Home AP*, 78(72), pp. 187-193.
- Chen, P., Kim, G.Y. & Ni, J. (2008). Fabrication of high aspect ratio porous micro-features using hot compaction technique. *Journal of Manufacturing Science and Engineering*, 130(3), pp. 0311031-0311038.
- Chicinas, I. (2006). Soft magnetic nanocrystalline powders produced by mechanical alloying routes. *Journal of Optoelectronics and Advanced Materials*, 8(2), pp. 439- 448.
- Chung, K.H., He, J., Shin, D.H. & Schoenung, J.M. (2003). Mechanisms of microstructure evolution during cryomilling in the presence of hard particles. *Materials Science and Engineering A*, 356 (1-2), pp. 23-31.
- Cullity, B.D. (1956). *Element of X-Ray Diffraction*. United State of America: Addison-Wesley Publishing Company, Inc.
- Dearnaley, G. (1969). Ion bombardment and implantation. *Reports on Progress in Physics*, 32(2), pp. 405-491.
- Dearnaley, G. (1974). Ion Implantation. *Annual Review of Materials Science*, 4, pp. 93-123.
- Denison, A.B., Hope-Weeks, L.J., Meulenberg, R.W. & Terminello, L.J. (2004). Quantum Dots, in *Introduction to Nanoscale Science and Technology*. In Di Ventra, M, Evoy, S, and Heflin, J.R (Eds.). *Springer Science & Business Media Inc.* pp. 183-198.
- Dheeradhada, V.S., Cao, H., Hearn, E.H., Wark, D.A. & Alinger, M.J. (2011). Oxidation of ferritic stainless steel Interconnects. *Journal of Power Sources*, 196(4), pp. 1975-1982.

- Eckert, J. & Borner, I. (1997). Nanostructure formation and properties of ball Milled Ni-Al intermetallic compound. *Material Science and Engineering A*, 239-240, pp. 619-624.
- El-Eskandarany, M.S. (2001). *Mechanical Alloying for Fabrication of Advanced Engineering Materials*. New York: William Andrew Publishing.
- Fergus, J.W. (2005). Metallic interconnects for solid oxide fuel cells. *Material Science and Engineering A*, 397(1-2), pp. 271-283.
- Godlewska, E., Szczepanik, S., Mania, R., Krawiarz, J. & Kozinski, S. (2003). FeAl materials from intermetallic powders. *Intermetallics*, 11, pp. 307-312.
- Grabke, H.J. & Horz, G. (1977). Kinetics and mechanisms of gas-metal reactions. *Annual Review of Materials Science*, 7, pp. 155-178.
- Griner, E.J. & Kock, H.W. (1994). In: *Proceedings of the first European solid oxide fuel cell forum*, Lucerne, Switzerland, 1, pp. 525.
- Haile, S.M. (2003). Fuel Cell Materials and components. *Acta Materialia*, 51(19), pp. 5981-6000.
- Han, M., Peng, S., Wang, Z., Yang, Z. & Chen, X. (2007). Properties of Fe-Cr based alloys as interconnects in a solid oxide fuel cell. *Journal of Power Sources*, 164, pp. 278-283.
- He, B.B. (2009). *Two-Dimensional X-Ray Diffraction*. New Jersey, Canada: John Wiley & Sons, Inc.
- Hilpert, K., Das, D., Miller, M., Peck, D. H. & Weiss, R. (1996). Chromium vapor species over solid oxide fuel interconnect materials and their potential for degradation processes. *Journal of the Electrochemical Society*, 143, pp. 3642-3647.